Title
Combined diffuse optical tomography (DOT) and MRI system for cancer imaging in small animals

Journal
Technology in Cancer Research & Treatment, 5(4)

ISSN
1533-0346

Authors
Gulsen, Gultekin
Birgul, Ozlem
Unlu, Mehmet Burcin
et al.

Publication Date
2006-08-01

Peer reviewed

Technology in Cancer Research and Treatment
ISSN 1533-0346
Volume 5, Number 4, August (2006)

Combined Diffuse Optical Tomography (DOT) and MRI System for Cancer Imaging in Small Animals

www.tcrt.org

Gultekin Gulsen, Ph.D.*
Ozlem Birgul, Ph.D.
Mehmet Burcin Unlu, Ph.D.
Roshanak Shafiiha, Ph.D.
Orhan Nalcioglu, Ph.D.

Tu and Yuen Center for
Functional Onco-Imaging
164 Irvine Hall
University of California
Irvine, California 92697, USA

Recently, there has been a great amount of interest in developing multi-modality imaging techniques for oncologic research and clinical studies with the aim of obtaining complementary information and, thus, improving the detection and characterization of tumors. In this present work, the details of a combined MR-diffuse optical imaging system for dual-modality imaging of small animals are given. As a part of this effort, a multi-spectral frequency domain diffuse optical tomography system is integrated with an MRI system. Here, a network analyzer provides the rf modulation signal for the laser diodes and measures the amplitude and the phase of the detected signals. Photomultiplier tubes are utilized to measure low-level signals. The integration of this optical imaging system with the 4T MRI system is realized by incorporating a fiber adaptive interface inside the MR magnet. Coregistration is achieved by a special probe design utilizing fiducial markers. A finite element algorithm is used to solve the diffusion equation and an inverse solver based on this forward solver is implemented to calculate the absorption and scattering maps from the acquired data. The MR *a priori* information is used to guide the optical reconstruction algorithm. Phantom studies show that the absorption coefficient of a 7 mm inclusion in an irregular object located in 64 mm phantom is recovered with 11% error when MR *a priori* information is used. ENU induced tumor model is used to test the performance of the system *in vivo*.

Keywords: Diffuse Optical Tomography; DOT; MRI; Multimodality; Animal Imaging; Cancer; and Reconstruction.

Introduction

The last decade has brought revolutionary new imaging techniques into cancer research and clinical practice. Along with accurate anatomical measurement techniques to detect and localize tumors, methods based on quantifying physiologic and metabolic properties are being developed. Optical imaging is one of these promising techniques and recent advances in the optical imaging field have focused on the transfer of techniques from laboratory to the clinic (1-11). Optical absorption and scattering coefficients are direct measures of tissue biochemical composition and morphology, and are true functional indicators of the tissue system. Specifically, optical absorption arises from the presence of specific biomolecules that absorb light at a particular wavelength. For near-infrared light, these biomolecules include hemoglobin, oxygenated-hemoglobin, water, and fat. Thus, an accurate quantitative measurement of optical absorption at multiple wavelengths in the near infrared provides the means to determine the absolute concentrations of these biomolecules within tissue. The hemoglobin concentration and oxygen saturation yield information about human cerebral activity. Together with water content and scattering parameter, they are also used for cancer detection (12-17). The total hemoglobin concentration of tumors

*Corresponding Author:
Gultekin Gulsen, Ph.D.
Email: ggulsen@uci.edu

were found to be three- to four-fold greater while the oxygen saturation levels were shown to be reduced compared to the normal tissue (18). These differences are due to the vessel formation in the tumors and the oxygen extraction demands of rapidly proliferating, metabolically active tumor cells. Moreover, tissue scattering may encode morphologic and pathophysiologic changes in tissue. It is believed that, the origin of the transport scattering coefficient is due to the differences in the index of refraction between the extracellular or cytoplasmic fractions of tissue and the lipid composition of the membranes bounding each cell and cellular organelle. Hence, variations in the scattering spectral features may indicate subcellular compositional changes in that matrix structure as a result of the invasion of diseased tissue into the surrounding stroma (9, 19-21).

Meanwhile, transgenic manipulation of small animals that are used as models of human diseases and pathological conditions together with the "reporter" gene technology have intensified the development of *in vivo* imaging systems for small animals (22-25). Initially, established imaging technologies such as MRI, CT, PET, and SPECT were adapted for small animal imaging. More recently, the optical imaging techniques have been applied for small animal imaging as well. The advance of fluorescence and bioluminescence reporter gene and reporter probe approaches allow the widespread utilization of fluorescence and bioluminescence imaging systems (26, 27). Although nuclear imaging (PET and SPECT), MR and CT are inherently tomographic imaging modalities, in most cases, the optical imaging has been accomplished with planar imaging systems that are unable to resolve depth and hence, have limited resolution. On the other hand, unlike the other modalities, planar optical imaging techniques provide a relatively simple, robust, cost-effective, and extremely sensitive means to image fundamental biological processes *in vivo*. To overcome the limitations of the planar imaging, tomographic methods have recently been applied in optical imaging with the help of the mathematical models that describe the photon propagation in the tissue and improved detection techniques (28-32). Two of these techniques, bioluminescence and fluorescence tomography, are intended to reconstruct 3D volumetric images that accurately localize signals and enable quantitative studies of bioluminescent sources and fluorescent contrast agents. The inverse problem in bioluminescent tomography that involves only internal light sources is more difficult compared to fluorescence tomography that uses external light source for excitation, *in vivo* applications of both techniques have already been demonstrated for small animal imaging (33-35).

In addition to these, the diffuse optical absorption and scattering tomography (DOT) has been also evaluated for small animal imaging. There have been a number of applications using DOT technique for small animal imaging (36-39). In addition to hemoglobin concentration, blood volume, and oxygen saturation, diffuse optical imaging techniques have also been applied for cerebral and tumor blood flow measurements (40-42). Lately, Xu *et al*. reported an MRI coupled broadband near-infrared (NIR) tomography system for small animal brain studies (43).

In this paper, we describe the development of an MRI coupled frequency domain near-infrared DOT system for cancer imaging in small animals. Although similar hybrid systems have been used for breast cancer imaging, to the best of our knowledge the combined MR-DOT system described in this manuscript is the first one dedicated for cancer imaging in small animals.

Frequency domain diffuse optical tomography uses arrays of sources and detectors to obtain spatially dependent optical parameters of tissue. Frequency-domain measurements provide information on the average photon path traveled in addition to the optical flux. This additional data provide uniqueness of the solution in recovering both coefficients simultaneously and allows the separation of absorption and scattering (44). Frequency domain systems require less expensive instrumentation compared to the time-resolved systems and have been successfully applied in imaging (44-48). To generate the absorption and scattering image, a finite element (FEM) reconstruction algorithm based on the diffusion equation is used (49-53). FEM models are versatile and applicable to complex geometries. This aspect of FEM makes it attractive for incorporating *a priori* information such as MR images. Generally, a Newton-type algorithm is used to obtain the solution that provides minimum error between the measured data and estimated measurements from the FEM forward solver. Since the number of measurements is significantly less than the number of elements of the FEM mesh constructed for modeling the imaging volume, the inverse problem is underdetermined. It is also ill posed and these properties of the inverse problem limit the spatial resolution and the accuracy of reconstructed optical parameters.

Multi-modality imaging systems such as combined DOT/MRI can provide complementary information and improve the characterization of tumors further. Magnetic resonance imaging and near-infrared diffuse optical tomography are two noninvasive techniques that provide complementary structural and functional physiological information. DOT can be used to obtain the chromophore concentration maps such as oxy- and deoxyhemoglobin, water, and fat whereas MRI provides high-resolution structural and functional information such as water, fat, and vascular volume. The FEM reconstruction algorithm for optical imaging requires the accurate knowledge of the boundary of the imaging volume. As a part of this combined system, MRI not only provides precise outer boundary of the imaging volume but also infor-

mation about the internal structures. The internal structure information can be used to divide the imaging volume into compartments and constrain the reconstruction process. It has been already shown that *a priori* structural information improves the accuracy of the model and makes the problem better determined by allowing the small number of measurements to be used in a more effective way (53-61).

Moreover, MRI may also provide water and fat concentrations, and vascular volume information that can be used to improve the reconstruction accuracy of the oxy- and deoxyhemoglobin and thus the detection and characterization of the tumor due to the associated vasculature. The DOT system acquires the data in tomographic geometry and photomultiplier tubes (PMTs) are used to detect sub-picowatt light levels that are typical for this geometry. Although PMTs provide higher sensitivity, their cut-off wavelength, which is around 850 nm, prohibits the accurate reconstruction of water and fat concentration from the measurements. Therefore, average bulk water and lipid content values are normally used for the concentration of these two chromophores. However, the accuracy of the reconstructed oxy- and deoxyhemoglobin concentrations can be improved by using water and fat concentrations obtained from MRI as *a priori* information for the optical reconstruction (60, 62).

Coregistration of these two methods has the potential to enhance our understanding of the complex biological processes associated with tumor transformation and growth. Ultimately, the combination of the two measurement techniques can be applied to monitoring tumor changes in response to therapy, resulting in an improved method to test cancer treatment efficacy. Previously, we had integrated a diffuse optical spectroscopy (DOS) system with MRI under collaboration with the Photon Migration Group directed by Dr. Tromberg (Beckman Laser Institute, UCI) for dual-modality measurements on small animals bearing tumors (61, 63, 64). In this work, we extended this dual-modality approach to tomographic imaging and built a small animal DOT system compatible to MR. Multi-compartmental solid and liquid phantoms were used to evaluate the performance of the system. Finally, ENU induced tumor model is used to test the performance of the system *in vivo*.

Materials and Methods

The design and construction of the combined MRI-DOT system, the details of data acquisition, phantom construction, and analysis are described in this section.

Instrumentation

Diffuse Optical Tomography (DOT): The details of the DOT system was previously given by Gulsen *et al*. (65). The

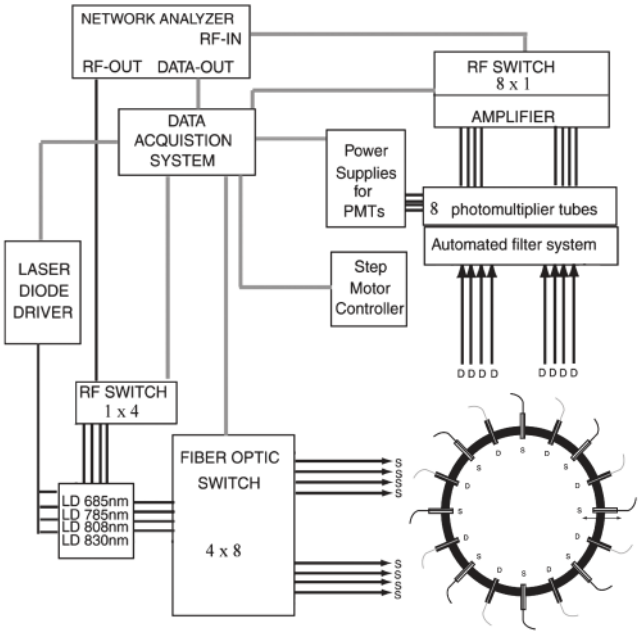

Figure 1: The schematic diagram of the multi-frequency DOT set-up.

DOT system is based on a network analyzer (Agilent Technologies, Palo Alto, CA), which measures the amplitude and the phase of the detected signals, and also provides the rf signal to modulate the amplitude of the laser diode sources. The network analyzer permits prompt selection of the modulation frequency between 100 MHz and 300 MHz. These limits are specific to our DOT system determined in the previous studies (65). Figure 1 shows the schematic of the DOT system. The system employs four different wavelengths, 665 nm (50 mW Intelite, Genoa, NV), 785 nm (75 mW, Thorlabs, Newton, NJ), 800 nm (150 mW Intelite, Genoa, NV), and 830 nm (100 mW Intelite, Genoa, NV). The laser diodes are driven by a DC current source (ILX Lightwave, Bozeman, MT). The laser diode outputs are multiplexed through the source fibers by a fiber optic switch (DICon Fiberoptic, Richmond, CA).

Photo multiplier tubes (PMT) are selected to measure low-level signals in fan-beam geometry. One PMT (R7400U-20 Hamamatsu, Japan) is used for each of the eight detection sites. The gain of each PMT can be adjusted individually and is determined at the beginning of an experiment. During an imaging session, the gain setting of each PMT is kept constant. A 1 × 8 RF switch (Hitite, Chelmsford, MA) and a 65 dB amplifier (Sonoma Instruments, Sonoma, CA) combination is used to multiplex and amplify the output of the PMTs.

The detectors nearest to the source receive orders of magnitude more incident light than those that are the farthest due to the detection geometry. Thus, either the light level or the gain of the PMT must be adjusted because of the limited dynamic range of the PMT. A filter wheel is used between the PMTs and fibers in the detection unit to reduce the dynamic range of

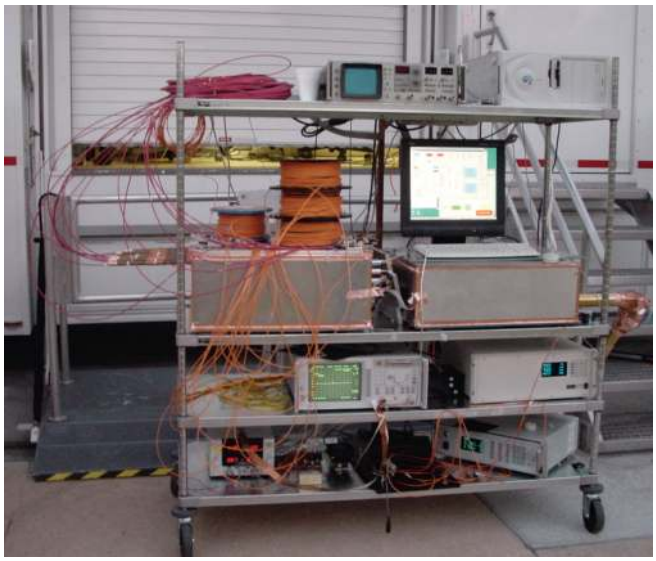

Figure 2: The picture of the DOT system

the measured light level. Therefore, the extensive dynamic range of the intensity measured from the sample is tuned to the dynamic range of the PMTs. This approach allows keeping the gain of each PMT at a certain value during the experiment and by making the calibration procedure easier, reduces any error that is potentially inherent in other types of calibration techniques. Keeping the PMT's bias voltage constant during the experiment decreases the voltage hysteresis while the neutral density filters limit the dynamic range of the light detected by the PMT thus, reducing the light hysteresis.

The PMTs, their high voltage power supplies, the rf switch, the filter wheel, and the rotation stage are all placed in a shielded aluminum box. The power supply lines for the circuits and the rotation stage, the control voltages for the high voltage power supplies, and the rf switch are filtered by feedthrough filters located on one side of the aluminum box. All of the DOT instruments were placed on a cart that allowed the transportation of the system from lab to the MRI facility that is in close proximity, Figure 2.

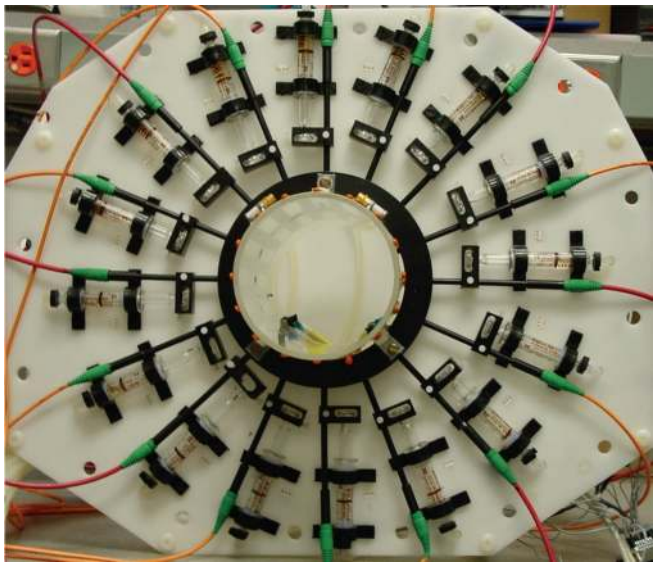

Figure 3: The new generation fiber optic interface. RF coil is fixed in the center of the fiber interface. Hydraulic actuators are used to move the fiber probes.

Integration with the Magnetic Resonance Imaging (MRI) System: The MRI system being used with the DOT is a homebuilt 4T human whole body scanner with a Marconi Medical, Inc. console. The bore diameter of the MRI is 94 cm, and a homebuilt birdcage rf coil for small animal is used to transmit and receive signals. To avoid the effects of fringe fields of the 4T magnet on the instrumentation, the DOT system is placed in a separate room, 15 m away from the magnet bore. Optical fibers are used to conduct light from the sources to the tissue as well as to transfer the collected light from tissue to detectors. Gradient index 62.5 μm core diameter fibers are used as the source fibers, while 1.1 mm core diameter step-index fibers are used as the detector fibers. The source and detector fibers are coupled to the animal RF coil inside the magnet. For this purpose, an

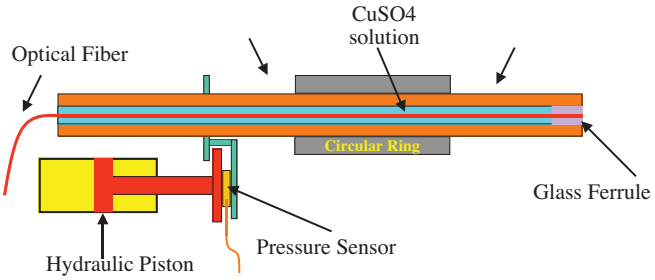

Figure 4: Fiber probes were machined in a cylindrical form with a center hole that contains the fiber. A computer controlled hydraulic actuators pushes the probes radially and a pressure sensor is utilized for each sensor to obtain the best contact quality.

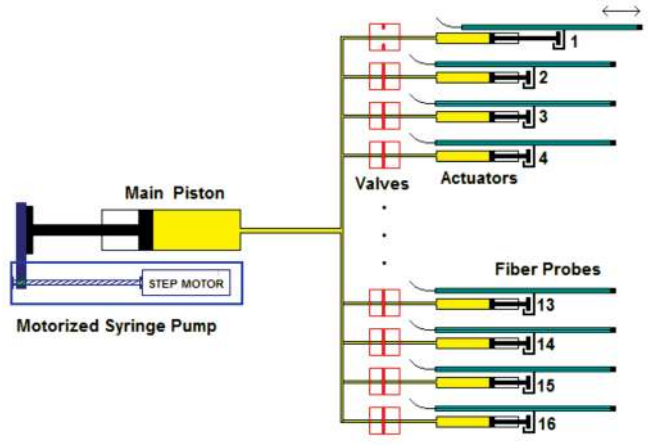

Figure 5: The computer controlled hydraulic system to activate the probes. The system is based on a main piston that is driven by computer. Sixteen solenoid valves are used to direct the hydraulic oil to any one of the actuators to be able to move a particular probe.

adaptive interface was constructed. It consists of 8-source and 8-detector fiber probes with radially adjustable holders. The RF coil is fixed in the center of the fiber interface and 16 holes are prepared for fiber probe entrances as seen in Figure 3. Fiber probes are machined in a cylindrical form with a center hole that contains the fiber. Custom made glass ferrules are used to fix and polish the tips of the fibers with the help of a polishing machine (Ultratec, Santa Ana, CA). After polishing, each ferrule was positioned at the end of each probe and glued. The center hole of the plastic probes is filled with H2O-CuSO4 solution to determine the location of the source and detector fibers in the MR images, Figure 4. A hydraulic system was implemented to move the probes radially, Figure 5. A computer controlled syringe pump was utilized to push or pull the main piston. Due to strong magnetic field, glass syringes were used as actuators for the optical probes. A series of hydraulic valves directed the hydraulic oil to a particular glass syringe. An electronic circuit board was implemented to control the hydraulic valves hence, the motion of the probes with computer. A separate sensor was used for each probe to measure the pressure applied to the tissue by the probe, Figure 4. The same circuit board also converts the amount of pressure to an electrical signal that is monitored by the computer. The pressure measurements were used as feedback to determine the final probe position and improve the probe-tissue contact.

Data Acquisition

The data is acquired simultaneously by both systems. Once the sample placed at the center of the fiber optic interface, the patient couch that holds the fiber interface is slid to position the interface at the center of the magnet bore. The imaging procedure includes three steps: (i) localization of the MRI slice that coincides with the optical imaging plane and beginning of DOT data acquisition; (ii) acquisition of T2-weighted anatomic MRI image; and (iii) calibration procedure for optical instrumentation, as shown in Figure 6. At the first step, the fast spin echo (FSE) sagital and coronal localizer pulse sequences are used to pinpoint the probes. At the same time, the DOT data acquisition is started. Later, an axial slice is chosen using the information obtained by the localizer sequences and tested for the coverage of all of the fiber probes in this 5 mm slice. In the next step, T2-weighted images using a fast spin-echo (FSE) sequence with TR/TE = 3000/15 ms, echo train = 8, field of view (FOV) = 10.5 cm, Image-Matrix = 256 × 256 and 5 mm in slice-thickness are acquired. After the DOT and the MRI acquisitions are completed, the sample is replaced with the homogeneous solid phantom and calibration measurements for the optical imaging system are done.

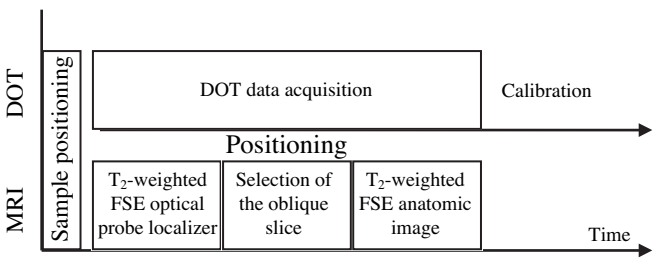

Figure 6: The imaging procedure includes three steps: (i) localization of the oblique MRI slice that coincides with the optical imaging plane and beginning of DOT data acquisition; (ii) T2-weighted anatomic MRI acquisition; (iii) optical instrumentation calibration.

Phantom Experiments

To test the performance of the system, multi-modality phantoms were constructed. Such a phantom must be constructed using suitable materials that are compatible and measurable by both modalities. To achieve this task, different circular, irregular solid shells and irregular solid compartments with circular holes simulating tissue optical properties were constructed by using the method described by Firbank *et al*. (66). The empty spaces between the compartments as well as the compartments themselves were filled with varying concentrations of Intralipid (%10, F. K. Clayton, Clayton, NC) and Indian ink (Winsor&Newton, England) in water. In addition to these, a 63 mm diameter solid homogeneous phantom was constructed using the same method. The optical properties of the homogeneous phantom were $\mu a = 0.013$ mm^{-1} and $\mu s' = 0.85$ mm^{-1} at 785 nm and used for calibration purposes.

The extinction coefficient of the Indian ink was determined by spectrophotometer. For this purpose, different concentrations of dye solutions were prepared and the absorption spectra of the solutions were measured. During the preparation of solid homogeneous phantoms, a cylindrical shell was also made using the same dye, microsphere, and epoxy solution. Hence, the optical properties of the solid shell were equal to the homogeneous solid phantom and calculated by fitting the homogeneous solid phantom data using the forward solver. Later, different concentrations of intralipid and In-

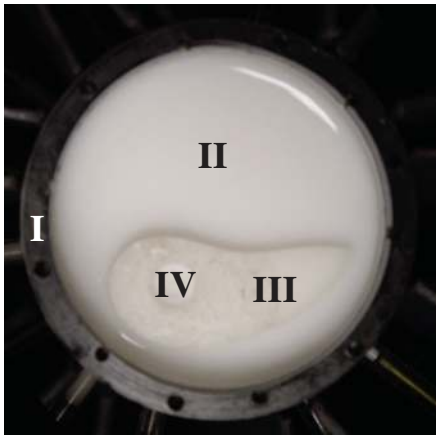

Figure 7: The picture of the multi-modality phantom. Four regions are indicated on the picture. (I) Shell; (II) Background; (III) Irregular shape; and (IV) 7mm circular inclusion.

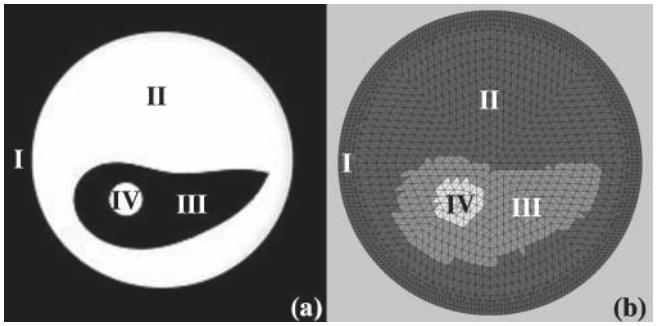

Figure 8: (**a**) The MR image of the multi-modality phantom, (**b**) The FEM mesh used for the reconstruction program. The elements that belong to different regions are color coded. The four regions are also numerically coded on the MR image and the FEM mesh: (I) Shell; (II) Background; (III) Irregular shape; and (IV) 7mm circular inclusion.

dian ink solutions were prepared. DOT measurements were acquired using the solid shell filled with these solutions. The absorption and scattering coefficients were again calculated by minimizing the difference between measured and estimated data. The dimensions and the optical properties of the solid shell were used as *a priori* information for the fitting algorithm. After all, the extinction coefficient of the Indian ink obtained by the spectrometer and DOT measurements agreed very well and the scattering coefficient obtained by DOT measurements were used as true values. The volumetric scattering of Intralipid and absorption of Indian ink per unit concentration were found to be 0.05 and 0.15 [mm^{-1} ml/l H_20] at 785 nm, respectively.

Figures 7 and 8(a) show the picture and the MR image of a multi-modality phantom, respectively. The four regions of the phantom are numerically coded in the Figures 7 and 8. These regions are the shell (I), the background (II), the irregular solid inclusion (III), and the 7mm circular object (IV). The absorption coefficient of the solid shell (I) and the intalipid/dye solution (II) were both set to 0.013 mm^{-1}. Then, a solid irregular inclusion (μa = 0.021 mm^{-1}) was placed in the phantom and fixed (III). The hole in this irregular inclusion (IV) was also filled with intalipid/dye solution and the absorption coefficient of this solution was set to 0.034 mm^{-1}. The reduced scattering coefficient of the shell and the intralipid/dye solutions were the same, $\mu s'$ = 0.85 mm^{-1}. The reduced scattering coefficient of the irregular object was lower, $\mu s'$ = 0.70 mm^{-1}. Later, a cap was placed on top of the phantom and sealed. Before the data acquisition, the phantom was placed in the fiber optic interface and positioned at the center of the MR bore. The data was acquired simultaneously with both MR and DOT systems following the protocol described in *Data Acquisition*. At the final stage, the multi-compartmental phantom was replaced with the solid homogeneous phantom and the calibration data was acquired before removing the fiber optic interface from the MR bore.

Animal Experiments

A carcinogen ENU (N-ethyl-N-nitrosourea) induced breast tumor model, which is known to induce benign tumors and malignant tumors with different grades is used to assess the performance of the combined system *in vivo*. As described by Stoica *et al*. (67), intraperitoneal administration of ENU to 30-day-old-female Sprague-Dawley rats results in a high incidence of mammary tumors that simulates human breast tumors. We have successfully established this model before (68). There is a definite dose-effect relationship. The rat is injected with 90 mg/kg ENU i.p. Based on this dose, 80% tumor incidence is expected and 65% of the induced tumors to be malignant. In general, the tumors show themselves three months after the injection. The early tumors are more likely to be malignant and the later tumors are likely to be benign.

The study was performed under an institutionally approved protocol. The animal was anesthetized with an intraperitoneal injection of 87mg/kg Ketamine and 13 mg/kg Xylazine, and placed in the fiber-optic interface. The position of the animal was adjusted to include tumor in the plane defined by the 16 fiber optic probes. The data was collected using 785 nm source and the modulation frequency was set to 110 MHz. The power incident on the tissue was nearly 50 mW.

Calibration of the Optical Imaging System

Calibration is crucial due to the variation in characteristics of each PMT, optical fiber, and neutral density filters. The calibration procedure for our DOT system includes filter, detector, and homogeneous phantom calibration steps and was given in detail previously (65). The first calibration step is done to find the optical density (OD) of each individual filter at different positions. The filters are used to reduce the dy-

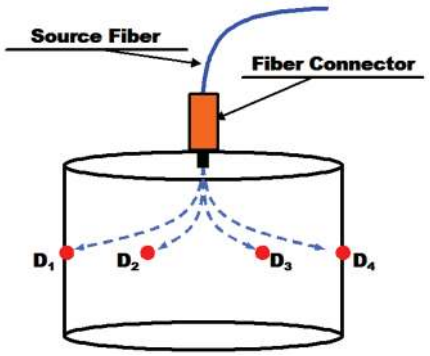

Figure 9: A homogeneous phantom is used for calibration. A separate source fiber is connectorized and a hole is precisely drilled at the center of the top surface of the phantom. The size of the hole is adjusted to snug fit the zirconium tip of the fiber connector. After the fiber connector is placed in the hole, measurements at each detector site is recorded for the homogeneous phantom calibration as described in *Calibration of the Optical Imaging System*.

namic range of the measured optical signals. The optical density of each filter is different and may vary from one position to another. The recorded OD values for each filter at different positions are used to calibrate the data obtained from a measurement set. In the second calibration step, each detection fiber is exposed to the same optical signal. For this purpose, a separate source fiber is connectorized and a hole is precisely drilled at the center of the top surface of the phantom. The size of the hole is adjusted to snug fit the zirconium tip of the fiber connector. After the fiber connector is placed in the hole, measurements at each detector site is recorded (69-71). Figure 9 shows the data acquisition scheme for the center calibration measurements. The amplitude and the phase measured by each channel may differ although they receive the same optical signal. These differences are recorded and used to calibrate the detector channel outputs. As a final step, a complete set of measurements from the homogeneous phantom is acquired. This calibration step is performed to account for the fiber differences in transmission and alignment and the discretization errors due to data/model mismatch (69).

Image Reconstruction

Given the calibrated photon density measurements, the next step is the calculation of the optical parameters inside the imaging region. In order to formulate the relation between the desired optical parameters and measurements, the diffusion equation in frequency domain is used (72, 73)

$$-\nabla \cdot \kappa(\vec{r})\nabla\Phi(\vec{r},\omega) + \left(\mu_a(\vec{r}) + \frac{i\omega}{c}\Phi(\vec{r},\omega)\right) = q_o(\vec{r},\omega), \quad \forall \vec{r} \in \Omega \qquad [1]$$

where $\Phi(\vec{r},\omega)$ is the photon density, $\mu_a(\vec{r})$ is the absorption coefficient, $\kappa(\vec{r}) = \{3(\mu_a(\vec{r}) + \mu'_s(\vec{r}))\}^{-1}$ is the diffusion coefficient, $\mu'_s(\vec{r})$ is the reduced scattering coefficient, $c = c_o/n$ is the speed of light, and n is the refractive index. The associated boundary condition is given as

$$\Phi(\xi) + \hat{a}_n \cdot 2\kappa(\xi)A\nabla\Phi(\xi) = 0, \qquad \forall \xi \in \partial\Omega \qquad [2]$$

where $\hat{a}_n$ is the outward normal to the boundary $\partial\Omega$ at ξ. Finite element method (FEM) is used for the solution of the boundary value problem defined above. The inverse problem is solved by minimizing the difference between measured and calculated data as explained in (72, 73). The solution can be written as

$$\Delta\mu = \left(J^T J + \lambda(\vec{r})I\right)^{-1} J^T(\phi_m - \phi_c), \qquad [3]$$

where J is the Jacobian matrix whose elements are calculated by the forward solver. ϕ_m and ϕ_c are the measured and the calculated data, respectively. We separate the complex valued frequency domain solution into its magnitude and phase components, scale them to have similar order of magnitudes, and use them simultaneously in the Jacobian matrix. For most cases, the number of measurements is considerably less than the number of unknowns, which is twice the number of elements in the finite element mesh, resulting in an underdetermined system. Moreover, Jacobian matrix is ill conditioned. Tikhonov regularization is a commonly used method to solve such problems (74). In Equation [3], $\lambda(\vec{r})$ is a region dependent regularization parameter (75) that is generated using the spatial *a priori* information from the MR image. Given the MR image, first the outer boundary information, probe locations, and boundaries of the interior region of interests are selected. Then, this information is superimposed on a finite element mesh and the elements corresponding to different regions are found. In this study, dual mesh approach is adopted where a mesh with 1761 nodes and 3264 first order triangular elements are used for forward calculations and a coarser mesh with 289 nodes and 512 elements is used for the Jacobian calculation. Finally, the resulting matrix equation is solved iteratively using a conjugate gradient solver to find the optical parameters. Note that homogeneous fitting is applied to the measured data at the beginning to determine the initial values for the iterative process. The mismatch in the refractive index due to the liquid inclusion in the solid phantom has been modeled in the FEM forward solver.

For comparison, reconstruction is done for with and without using the *a priori* information obtained from the MRI. In the first case, the sample is assumed to be homogeneous and a single regularization parameter is used for the whole imaging area. In the latter case, the imaging area is divided into sections using the MR image as explained in the previous part. Different regularization parameters are assigned for each section such that a lower regularization parameter is selected in a region of interest compared to the background (75). First, a ratio is set for each region and a single regularization parameter is found using a minimization algorithm. The optimal regularization value is selected as the one minimizing the difference,

$$\min_\lambda \sum_i^K \left\| \phi_{m,i} - \phi_{c,i}(\mu(\lambda)) \right\|$$

Where K is the total number of measurements, ϕ_c and ϕ_m are the calculated and measured fluences at the boundary, respectively. During the optimization, the regularization parameter is multiplied by these predetermined ratios before applied to each region. The ratio that belongs to each section is determined by simulation studies for a particular case.

Results

For the phantom experiments the modulation frequency was set to 110 MHz. Once the DOT data was calibrated using the homogeneous phantom measurements, the reconstruction program was used to generate the absorption and scattering maps

Table I

The true, mean, and standard deviation of the recovered absorption and scattering values for each region in the phantom. Regions #1, 2, 3, and 4 represent the shell, background (BG), irregular object (IO), and the 7mm circular object (inclusion), respectively.

	Actual	Without A Priori Info			With A Priori Info		
Region	μa (mm^{-1})	Mean μa (mm^{-1})	STD (mm^{-1})	Error (%)	Mean μa (mm^{-1})	STD (mm^{-1})	Error (%)
1-shell	0.013	0.015	0.004	17%	0.015	0.003	17%
2-B.G.	0.013	0.015	0.004	17%	0.015	0.003	17%
3-IO	0.021	0.024	0.005	15%	0.024	0.005	12%
4-inclusion	0.034	0.027	0.004	20%	0.030	0.007	11%

	Actual	Without A Priori Info			With A Priori Info		
Region	μs (mm^{-1})	Mean μs (mm^{-1})	STD (mm^{-1})	Error (%)	Mean μs (mm^{-1})	STD (mm^{-1})	Error (%)
1-shell	0.85	0.801	0.182	6%	0.785	0.124	8%
2-B.G.	0.85	0.801	0.182	6%	0.785	0.124	8%
3-IO	0.70	0.726	0.221	4%	0.737	0.197	5%
4-inclusion	0.85	0.730	0.145	14%	0.719	0.295	15%

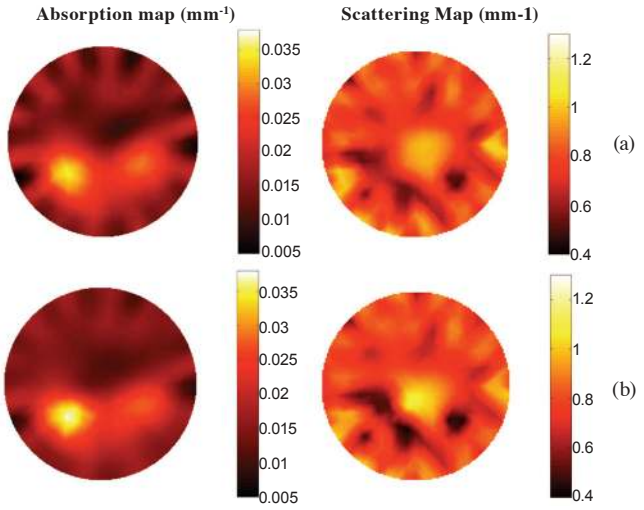

Figure 10: The reconstructed absorption and scattering coefficient maps without (**a**) and with (**b**) MRI *a priori* information. The error for the 7 mm small object was nearly 20% for the recovered absorption coefficient and reduced down to 11% with *a priori* information. For the irregular region, the mean absorption coefficient was recovered with 15% and 12% error without and with *a priori* information, respectively.

with and without *a priori* data. The location of the probes and the boundary of the irregular inclusion were obtained from the MR image, Figure 8(a). For the first case a single regularization parameter was employed for the whole imaging area. For the latter case, the boundary of the internal structures found using the MR image and the imaging area were divided into four sections: the shell (I), the background (II), the irregular inclusion (III), and the small 7 mm circular inclusion (IV). The background region was defined as the area between the solid shell and the irregular object that was filled with the intralipid/dye solution. The solid structures, the shell and the irregular inclusion, were not visible in the MR image. The irregular object was surrounded by the solution and its boundary could be extracted easily from the MR image. Although the outer boundary of the solid shell was not visible in the MR image, the knowledge of the inner boundary and the thickness enough to calculate the boundary of the phantom. For this case, the elements of the mesh that belong to each region were identified and recorded. Figure 8(b) shows the fine mesh used to solve the forward problem. The elements were color and numerically coded to present the selection of elements for each of the four sections. Later, the regularization parameter for each section was assigned as described in *Image Reconstruction*. For this particular phantom the same regularization parameter was assigned to the shell and the background regions. The optimum ratios found by the simulations were 1.0, 1.0, 0.6, and 0.3 for the shell (region #1), background (region #2), irregular object (region #3), and 7mm circular object (region #4), respectively. Once these ratios were chosen, a minimization method was used to find the best lambda values for each region to minimize the difference between the measurements and the forward problem solution.

Figures 10(a) and 10(b) show the reconstructed absorption and scattering maps without and with *a priori* MR infor-

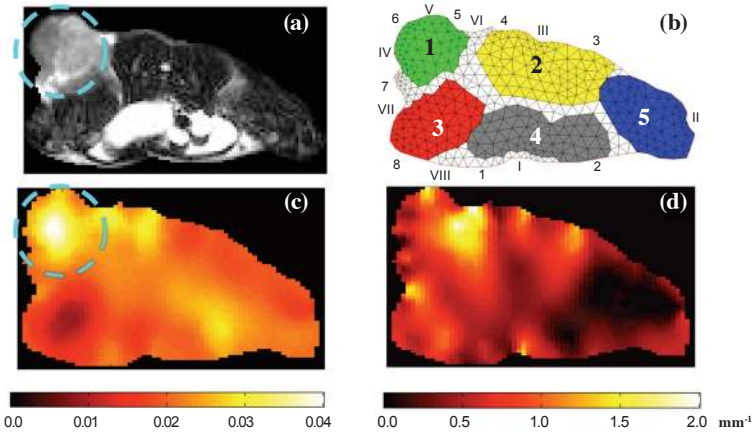

Figure 11: (**a**) The MR anatomical image. (**b**) The FEM mesh constructed based on the MR image. Numbers (1-8) on the mesh indicates the source fiber locations and (I-VIII) are the detector fiber locations. The areas corresponding to the tumor, the back muscle, and the bladder are indicated as region #1, #2, and #4 on FEM mesh. The muscle located on the left and right-hand sides are indicated as region #3 and #5. (**c**) The reconstructed absorption map. (**d**) The reconstructed scattering map. The size of the tumor was approximately 1.5 cm and is indicated by the dashed circle in the upper left side of the image. It is seen that, there is nearly a two-fold increase in the absorption around the tumor.

mation, respectively. It is seen that the utilization of MR *a priori* information improves the reconstruction results.Table I summarizes the results giving the true, mean, and standard deviation of the recovered absorption and scattering values for each region with and without *a priori* information. As seen from Figure 10(a), the error in the recovered mean absorption coefficient of the irregular and 7mm circular object was 15% and 20%, respectively. However, the mean absorption value of the 7mm object were recovered better using the MR *a priori* information. The recovered value for this small object located in the irregular object increased from 0.027 mm^{-1} to 0.030 mm^{-1} when the reconstruction algorithm was guided by the MR structural information. Therefore, the error in the recovered mean value for this object was reduced down to 11% based on the true value of 0.034 mm^{-1}. In addition to these, the FWHM of the small object measured from the recovered absorption map was 10.5 mm and 11.5 mm with and without MR *a priori* information, respectively. A similar improvement was observed for the irregular object as well. The mean absorption coefficient of the irregular object was recovered with 12% error when the imaging volume was divided into several sections and different regularization parameters were assigned to these sections.

Later, the performance of the system was assessed *in vivo* using a rat bearing ENU tumor. Figure 11(a) shows the MR anatomical image. The size of the tumor was approximately 1.5 cm and it is clearly seen in the upper left side of the image. First, the boundary of the animal was extracted from the MR image and used to generate FEM mesh. Later, the probe positions were found with the help of the CuSO4 solutions and co-registered with the FEM mesh. For the forward solver, a fine mesh with 1649 nodes and 3072 triangular elements and for the inverse problem, a coarse mesh [Figure 11(b)] with 441 nodes and 768 elements was generated. Numbers (1-8) on the mesh indicates the source fiber locations and (I-VIII) are the detector fiber locations. Figure 11(c) and 11(d) show the absorption and scattering maps reconstructed using this mesh. The areas corresponding to the tumor, the back muscle, and the bladder are indicated as region #1, #2, and #4 on FEM mesh, Figure 11(b). Moreover, the muscle located on the left and right-hand sides are indicated as region #3 and #5. The true, mean, and standard deviation of the recovered absorption and scattering values for each region are given in the Table II. It is seen that there is nearly a two-fold increase in the absorption around the tumor. Scattering also increases in this area, however, the increase mostly occurs on the inner boundary of the tumor.

Table II

The true, mean, and standard deviation of the recovered absorption and scattering values for each region in the animal. The areas corresponding to the tumor, the back muscle, and the bladder are indicated as region #1, #2, and #4, respectively, while the muscle located on the left and right-hand sides are indicated as region #3 and #5.

	$\mu a\,(mm^{-1})$			$\mu s\,(mm^{-1})$		
Region #	Max	Mean	Std	Max	Mean	Std
1-tumor	0.044	0.027	0.005	2.690	0.838	0.512
2-back muscle	0.034	0.023	0.004	2.391	0.667	0.369
3-muscle left	0.024	0.016	0.004	1.896	0.735	0.251
4-bladder	0.031	0.021	0.003	1.007	0.405	0.243
5-muscle right	0.025	0.020	0.002	0.842	0.250	0.255

Discussion

The implementation of a combined MR-DOT system has been realized. Our prototype system uses a network analyzer, which is an expensive instrument. However, it could be replaced by a heterodyne circuit board that converts rf modulation frequencies into audio frequency range prior to record with a low cost data acquisition system. The amplitude and phase information could be calculated later during the post-processing of the data. This data acquisition scheme would reduce the cost of the system drastically. We have been already working on such a scheme and planning to implement it for the next generation of our DOT system.

The performance of the system tested with phantom and *in vivo* studies. Phantom experiments revealed the improvement in the accuracy of the recovered optical parameters with the use of *a priori* data as demonstrated in the literature (53-61). A complex phantom was designed to simulate a more realistic case. A 7 mm object was embedded in another object whose boundary was irregular. This small object located in an irregular inclusion can be recovered better if the reconstruction algorithm is guided by the information about the boundary of the internal structures obtained from MRI. The error in the recovered mean absorption coefficient of the 7 mm object embedded in this irregular compartment was reduced from 20% down to 11% with the structural *a priori* information. Moreover, MRI information also improved the recovered mean absorption value for the irregular object. We believe one of the reasons of the low quality scattering image is that there is no scattering contrast between the regions. The scattering values of all compartments were very close to each other. Due to this reason, fluctuations in the scattering images were higher than the absorption images and no improvement was observed in the recovered scattering maps. The second reason could be the choice of the materials used in the phantom reconstruction. We used solid shell and irregular objects, and liquid intralipid-dye mixture for the background and the 7 mm circular object. The index of refraction mismatch at the interfaces of these sections could lead to errors in the recovered scattering coefficients as well. Please note the low errors in the recovered optical properties even without *a priori* information. These results also indicate that a more complex phantom would enhance the effect of MRI *a priori* information. For example, Brooksby *et*

al. used a 82 cm diameter phantom with two layers and 2.2 cm cylindrical inclusion placed in the inner layer (59). They demonstrated that when *a priori* information is used, the rms error in the absorption and scattering reduces down to 43% and 55% for the inclusion, respectively. In our phantom study, the error for the 7 mm small object was nearly 20% for the recovered absorption coefficient and reduced down to 11% with *a priori* information. On the other hand, the error in the scattering coefficient did not reduce. We are working on gelatin phantoms to eliminate the effect of index of refraction mismatch and improve the reconstruction quality.

The feasibility of the system was also tested with an animal study. The tumor region (#1) had the highest absorption. The peak absorption in this region was 0.44 mm^{-1} while the peak absorption in regions #2, 3, and 5 were 0.34, 0.24 and 0.25 mm^{-1}, respectively. The tumor region also had high scattering, mostly on the inner boundary of the tumor. In the rat, ENU induces primarily infiltrating ductal carcinoma (IDC) breast cancer (as in humans), and also primarily fibroadenoma (FA) benign breast tumors (also as in humans) (67). ENU induced rat breast IDCs also show a range of morphological changes, from well-differentiated proliferations of tubules with minimal stromal invasion to highly infiltrative, poorly differentiated, and rapidly dividing tumors. Su *et al*. compared the degrees of aggressiveness among the malignant tumors with the MRI characteristics of different contrast agents (68). For example, as in humans, the kinetics of Gd-DTPA in ENU induced FAs have been reported to show a slower up-slope and a slower decay rate than that in malignant tumors (76). Besides, ENU induces FAs found to have a lower vascular volume and a higher interstitial space volume than ENU induced IDCs. In summary, these findings also supported that the properties of ENU tumors are similar to the human breast tumors. In the meantime, depending on the type and the aggressiveness of the tumor, the vascular volume and the absorption of the tumor would be different. In our previous MR-DOS studies, the absorption and scattering coefficient of the R3230 AC adenocarcinoma rat tumors were found around 0.013 mm^{-1} and 2 mm^{-1} at 785 nm, respectively (63, 64). However, in those studies the data was collected using a single source-detector pair separated by 5.7 mm and an average value found for the probed volume. The limited probing depth and the different tumor type could account for the differences in the recovered values for tumor with our DOT instrumentation. Moreover, using source-detector separation of 9.45 mm, Pham *et al*. reported absorption and scattering values of 0.0374 mm^{-1} and 0.86 mm^{-1} for subcutaneous rat ovarian cancer tumor at 811 nm, respectively (77). These values are in good agreement with the mean absorption and scattering values recovered for the tumor in our study, 0.027 mm^{-1} and 0.838 mm^{-1} (Table II).

The region #4 covered the internal organs such as the bladder and possibly intestines that are full of liquid that give higher signal in the T2 weighted anatomic image. The scattering value for this region was expected to be low due to the vast amount of water. Indeed, the mean scattering coefficient for this region was found as 1.0 mm^{-1}, low compared to the other regions. The only exception was the region #5 that covers the muscle on the right hand side of the animal. It is possible that the diffusion approximation fails for region #4 that covers the bladder and gives inaccurate result for this region. There are a couple of reports about the effect of non-scattering regions on diffusion-approximation-based image reconstruction (78-80). Xu *et al*. demonstrated that the recovered absorption coefficient for non-scattering targets in a scattering background is unphysically low, while the target location, size, and the general shape of absorption images are quantitatively accurate (80). They concluded that the diffusion approximation model may still be used for reconstructing optical images involving small non- and low scattering regions. The close proximity of region #5 to this region combined with the sparse sampling, only single detector site corresponding to region #5, might be the reason for the unexpected low scattering value recovered for this region.

These first *in vivo* results obtained from the hybrid imaging system demonstrates the potential of this system for cancer imaging in small animals. In the future studies, we are planning to implement RTE based FEM reconstruction algorithm to eliminate the artifacts due to the low scattering regions as demonstrated by Gassan *et al*. (81). In addition to this, we are also planning to extend our approach to obtain chromophore maps (11) and to use functional MRI information such as fat, water, and blood vascular volume information to guide the reconstruction algorithm better (68, 82). Such a combined system can also be used to monitor the enhancement kinetics of MRI and optical exogenous agents simultaneously to enhance the information obtained content (83).

Acknowledgments

The authors express thanks to Hon Yu for performing the MR data acquisition. This research is funded by the National Cancer Institute through Grant # P20 CA86182 and R21/33 CA-101139.

References

1. Culver, J. P., Choe, R., Holboke, M. J., Zubkov, L., Durduran, T., Slemp, A., Ntziachristos, V., Chance, B., Yodh, A. G. Three-dimensional Diffuse Optical Tomography in the Parallel Plane Transmission Geometry: Evaluation of a Hybrid Frequency Domain/Continuous Wave Clinical System for Breast Imaging. *Med. Phys. 30*, 235-247 (2003).
2. Schmitz, C. H., Klemer, D. P., Hardin, R., Katz, M. S., Pei, Y., Graber, H. L., Levin, M. B., Levina, R. D., Franco, N. A., Solomon, W. B., Barbour, R. L. Design and Implementation of Dynamic Near-infrared Optical Tomographic Imaging Instrumentation for Simultaneous Dual-breast Measurements. *Appl. Opt. 44*, 2140-2153 (2005).
3. Dehghani, H., Pogue, B. W., Poplack, S. P., Paulsen, K. D. Multi-wavelength Three-dimensional Near-infrared Tomography of the

Breast: Initial Simulation, Phantom, and Clinical Results. *Appl. Opt. 42*, 135-145 (2003).
4. Franceschini, M. A., Moesta, K. T., Fantini, S., Gaida, G., Gratton, E., Jess, H., Mantulin, W. W., Seeber, M., Schlag, P. M., Kaschke, M. Frequency-domain Techniques Enhance Optical Mammography: Initial Clinical Results. *Proc. Natl. Acad. Sci. USA 94*, 6468-6473 (1997).
5. Godavarty, A., Eppstein, M. J., Zhang, C., Sevick-Muraca, E. M. Detection of Single and Multiple Targets in Tissue Phantoms with Fluorescence-enhanced Optical Imaging: Feasibility Study. *Radiology. 235*, 148-154 (2005).
6. Grosenick, D., Wabnitz, H., Moesta, K. T., Mucke, J., Moller, M., Stroszczynski, C., Stossel, J., Wassermann, B., Schlag, P. M., Rinneberg, H. Concentration and Oxygen Saturation of Haemoglobin of 50 Breast Tumours Determined by Time-domain Optical Mammography. *Phys. Med. Biol. 49*, 1165-1181 (2004).
7. Intes, X., Ripoll, J., Chen, Y., Nioka, S., Yodh, A. G., Chance, B. *In Vivo* Continuous-wave Optical Breast Imaging Enhanced with Indocyanine Green. *Med. Phys. 30*, 1039-1047 (2003).
8. Pera, V. E., Heffer, E. L., Siebold, H., Schutz, O., Heywang-Kobrunner, S., Gotz, L., Heinig, A., Fantini, S. Spatial Second-derivative Image Processing: An Application to Optical Mammography to Enhance the Detection of Breast Tumors. *J. Biomed. Opt. 8*, 517-524 (2003).
9. Pogue, B. W., Jiang, S., Dehghani, H., Kogel, C., Soho, S., Srinivasan, S., Song, X., Tosteson, T. D., Poplack, S. P., Paulsen, K. D. Characterization of Hemoglobin, Water, and NIR Scattering in Breast Tissue: Analysis of Intersubject Variability and Menstrual Cycle Changes. *J. Biomed. Opt. 9*, 541-552 (2004).
10. Jakubowski, D. B., Cerussi, A. E., Bevilacqua, F., Shah, N., Hsiang, D., Butler, J., Tromberg, B. J. Monitoring Neoadjuvant Chemotherapy in Breast Cancer using Quantitative Diffuse Optical Spectroscopy: A Case Study. *J. Biomed. Opt. 9*, 230-238 (2004).
11. Li, A., Zhang, Q., Culver, J. P., Miller, E. L., Boas, D. A. Reconstructing Chromosphere Concentration Images Directly by Continuous-wave Diffuse Optical Tomography. *Opt. Lett. 29*, 256-258 (2004).
12. McBride, T. O., Pogue, B. W., Poplack, S., Soho, S., Wells, W. A., Jiang, S., Osterberg, U. L., Paulsen, K. D. Multispectral Near-infrared Tomography: A Case Study in Compensating for Water and Lipid Content in Hemoglobin Imaging of the Breast. *J. Biomed. Opt. 7*, 72-79 (2002).
13. Boas, D. A., Gaudette, T., Strangman, G., Cheng, X., Marota, J. J., Mandeville, J. B. The Accuracy of Near Infrared Spectroscopy and Imaging During Focal Changes in Cerebral Hemodynamics. *Neuroimage 13*, 76-90 (2001).
14. Gratton, E., Toronov, V., Wolf, U., Wolf, M., Webb, A. Measurement of Brain Activity by Near-infrared Light. *J. Biomed. Opt. 10*, 11008 (2005).
15. Grosenick, D., Wabnitz, H., Moesta, K. T., Mucke, J., Schlag, P. M., Rinneberg, H. Time-domain Scanning Optical Mammography: II. Optical Properties and Tissue Parameters of 87 Carcinomas. *Phys. Med. Biol. 50*, 2451-2468 (2005).
16. Ntziachristos, V., Chance, B. Probing Physiology and Molecular Function Using Optical Imaging: Applications to Breast Cancer. *Breast Cancer Res. 3*, 41-46 (2001).
17. Cerussi, A. E., Jakubowski, D., Shah, N., Bevilacqua, F., Lanning, R., Berger, A. J., Hsiang, D., Butler, J., Holcombe, R. F., Tromberg, B. J. Spectroscopy Enhances the Information Content of Optical Mammography. *J. Biomed. Opt. 7*, 60-71 (2002).
18. Tromberg, B. J., Shah, N., Lanning, R., Cerussi, A., Espinoza, J., Pham, T., Svaasand, L., Butler, J. Non-invasive *In Vivo* Characterization of Breast Tumors Using Photon Migration Spectroscopy. *Neoplasia. 2*, 26-40 (2000).
19. Blyschak, K., Simick, M., Jong, R., Lilge, L. Classification of Breast Tissue Density by Optical Transillumination Spectroscopy: Optical and Physiological Effects Governing Predictive Value. *Med. Phys. 31*, 1398-1414 (2004).
20. Srinivasan, S., Pogue, B. W., Jiang, S., Dehghani, H., Kogel, C., Soho, S., Gibson, J. J., Tosteson, T. D., Poplack, S. P., Paulsen, K. D. Interpreting Hemoglobin and Water Concentration, Oxygen Saturation, and Scattering Measured *In Vivo* by Near-infrared Breast Tomography. *Proc. Natl. Acad. Sci. USA 100*, 12349-12354 (2003).
21. Pogue, B. W., Song, X., Srinivasan, S., Dehghani, H., Paulsen, T. D., Tosteson, K. D., Kogel, C., Soho, S., Poplack, S. Near-infrared Scattering Spectrum Differences Between Benign and Malignant Breast Tumors Measured *In Vivo* with Diffuse Tomography. *OSA Biomedical Optics Topical Meetings, Technical Digest*. ThB1 (2004).
22. Hielscher, A. H. Optical Tomographic Imaging of Small Animals. *Curr Opin Biotechnol. 16*, 79-88 (2005).
23. Ntziachristos, V., Ripoll, J., Wang, L. V., Weissleder, R. Looking and Listening to Light: The Evolution of Whole-body Photonic Imaging. *Nat. Biotechnol. 23*, 313-320 (2005).
24. Piwnica-Worms, D., Schuster, D. P., Garbow, J. R. Molecular Imaging of Host-pathogen Interactions in Intact Small Animals. *Cell Microbiol. 6*, 319-331 (2004).
25. Gibson, A. P., Hebden, J. C., Arridge, S. R. Recent Advances in Diffuse Optical Imaging. *Phys. Med. Biol. 50*, R1-43 (2005).
26. Contag, C. H., Bachmann, M. H. Advances in *In Vivo* Bioluminescence Imaging of Gene Expression. *Annu. Rev. Biomed. Eng. 4*, 235-260 (2002).
27. Weissleder, R., Ntziachristos, V. Shedding Light onto Live Molecular Targets. *Nat. Med. 9*, 123-128 (2003).
28. Graves, E. E., Weissleder, R., Ntziachristos, V. Fluorescence Molecular Imaging of Small Animal Tumor Models. *Curr. Mol. Med. 4*, 419-430 (2004).
29. Weissleder, R. Scaling Down Imaging: Molecular Mapping of Cancer in Mice. *Nat. Rev. Cancer. 2*, 11-18 (2002).
30. Klose, A. D., Hielscher, A. H. Fluorescence Tomography with Simulated Data Based on the Equation of Radiative Transfer. *Opt. Lett. 28*, 1019-1021 (2003).
31. Dehghani, H., Davis, S. C., Jiang, S., Pogue, B. W., Paulsen, K. D., Patterson, M. S. Spectrally Resolved Bioluminescence Optical Tomography. *Opt. Lett. 31*, 365-367 (2006).
32. Wang, G., Li, Y., Jiang, M. Uniqueness Theorems in Bioluminescence Tomography. *Med. Phys. 31*, 2289-2299 (2004).
33. Ntziachristos, V., Schellenberger, E. A., Ripoll, J., Yessayan, D., Graves, E., Bogdanov, A., Jr., Josephson, L., Weissleder, R. Visualization of Antitumor Treatment by Means of Fluorescence Molecular Tomography with an Annexin V-Cy5.5 Conjugate. *Proc. Natl. Acad. Sci. USA 101*, 12294-1229 (2004).
34. Chaudhari, A. J., Darvas, F., Bading, J. R., Moats, R. A., Conti, P. S., Smith, D. J., Cherry, S. R., Leahy, R. M. Hyperspectral and Multispectral Bioluminescence Optical Tomography for Small Animal Imaging. *Phys. Med. Biol. 50*, 5421-5441 (2005).
35. Hwang, K., Houston, J. P., Rasmussen, J. C., Joshi, A., Ke, S., Li, C., Sevick-Muraca, E. M. Improved Excitation Light Rejection Enhances Small-animal Fluorescent Optical Imaging. *Mol. Imaging. 4*, 194-204 (2005).
36. Culver, J. P., Durduran, T., Furuya, D., Cheung, C., Greenberg, J. H., Yodh, A. G. Diffuse Optical Tomography of Cerebral Blood Flow, Oxygenation, and Metabolism in Rat During Focal Ischemia. *J. Cereb. Blood Flow Metab. 23*, 911-924 (2003).
37. Schmitz, C. H., Stewart, M., Farber, M. , Graber, H. L., Levina, R. D., Levin, M. B., Pei, Y., Xu, Y., Barbour, R. L. Dynamic Studies of Small Animals with a Four-color DOT Imager. *Rev. Sci. Instrum. 76,* 0904302 (2005).
38. Bluestone, A. Y., Stewart, M., Lasker, J., Abdoulaev, G. S., Hielscher, A. H. Three-dimensional Optical Tomographic Brain Imaging in Small Animals, Part 1: Hypercapnia. *J. Biomed. Opt. 9*, 1046-1062 (2004).
39. Chen, Y., Intes, X., Tailor, D. R., Regatte, R. R., Ma, H., Ntziachristos, V., Leigh, J. S., Reddy, R., Chance, B. Probing Rat Brain Oxygenation

with Near-infrared Spectroscopy (NIRS) and Magnetic Resonance Imaging (MRI). *Adv. Exp. Med. Biol. 510,* 199-204 (2003).
40. Yuan, S., Devor, A., Boas, D. A., Dunn, A. K. Determination of Optimal Exposure Time for Imaging of Blood Flow Changes With Laser Speckle Contrast Imaging. *Appl. Opt. 44*, 1823-1830 (2005).
41. Dunn, A. K., Devor, A., Dale, A. M., Boas, D. A. Spatial Extent of Oxygen Metabolism and Hemodynamic Changes During Functional Activation of the Rat Somatosensory Cortex. *Neuroimage. 27*, 279-290 (2005).
42. Zhou, C., Yu, G., Daisuke, F., Greenberg, J. H., Yodh, A. G., Durduran, T. Diffuse Optical Correlation Tomography of Cerebral Blood Flow During Cortical Spreading Depression in Rat Brain. *Optics Express 14*, 1125-1144 (2006).
43. Xu, H., Springett, R., Dehghani, H., Pogue, B. W., Paulsen, K. D., Dunn, J. F. Magnetic-Resonance-Imaging-Coupled Broadband Near-infrared Tomography System for Small Animal Brain Studies. *Appl. Opt. 44*, 2177-2188 (2005).
44. Chance, B., Cope, M., Gratton, E., Ramanujam, N., Tromberg, B. Phase Measurement of Light Absorption and Scatter in Human Tissue. *Rev. Sci. Inst. 69*, 3457-3481 (1998).
45. Gurfinkel, M., Pan, T., Sevick-Muraca, E. M. Determination of Optical Properties in Semi-infinite Turbid Media Using Imaging Measurements of Frequency-domain Photon Migration Obtained With an Intensified Charge-coupled Device. *J. Biomed. Opt. 9*, 1336-1346 (2004).
46. Fantini, S., Franceschini, M. A., Gaida, G., Gratton, E., Jess, H., Mantulin, W. W., Moesta, K. T., Schlag, P. M., Kaschke, M. Frequency-domain Optical Mammography: Edge Effect Corrections. *Med. Phys. 23*, 149-157 (1996).
47. McBride, T. O., Pogue, B. W., Jiang, S., Österberg, U. L., Paulsen, K. D. A Parallel-detection Frequency-domain Near-infrared Tomography System for Hemoglobin Imaging of the Breast *In Vivo*. *Rev. Sci. Inst. 72,* 1817-1824 (2001).
48. Srinivasan, S., Pogue, B. W., Jiang, S., Dehghani, H., Kogel, C., Soho, S., Gibson, J. J., Tosteson, T. D., Poplack, S. P., Paulsen, K. D. *In Vivo* Hemoglobin and Water Concentrations, Oxygen Saturation, and Scattering Estimates from Near-infrared Breast Tomography Using Spectral Reconstruction. *Acad. Radiol. 13*, 195-202 (2006).
49. Jiang, H., Paulsen, K. D., Osterberg, U. L., Patterson, M. S. Frequency-domain Near-infrared Photo Diffusion Imaging: Initial Evaluation in Multitarget Tissuelike Phantoms. *Med. Phys. 25*, 183-193 (1998).
50. Dyczij-Edlinger R, P. G. a. L .J. Efficient Finite Element Solvers for the Maxwell Equations in the Frequency Domain. *Comp. Metod. Appl. Mech. Eng. 169,* 297-309 (1999).
51. Hebden, J. C., Veenstra, H., Dehghani, H., Hillman, E. M., Schweiger, M., Arridge, S. R., Delpy, D. T. Three-dimensional Time-Resolved Optical Tomography of a Conical Breast Phantom. *Appl. Opt. 40*, 3278-3287 (2001).
52. Pogue, W., Geimer, S., McBride, T., Jiang, S., Osterberg, U. L., Paulsen, K. D. 3-D Simulation of Near-infrared Diffusion in Tissue: Boundary Conditions and Geometry Analysis for a Finite Element Reconstruction Algorithm. *Appl. Opt. 40,* 588-600 (2001).
53. Pogue, B. W., Paulsen, K. High-resolution Near-infrared Tomographic Imaging Simulations of the Rat Cranium by Use of *A Priori* Magnetic Resonance Imaging Structural Information. *Optics Letters 23,* 1716-1718 (1998).
54. Pei, Y., Lin, F. B., Barbour, R. Modeling of Sensitivity and Resolution to an Included Object in Homogeneous Scattering Media and in MRI-derived Breast Maps. *Optics Express 5,* 203-219 (1999).
55. Hielscher, A., Alcouffe, R., Barbour, R. Transport and Diffusion Calculations on MRI-generated Data. *Proceedings of SPIE 2979,* 500 (1997).
56. Ntziachristos, V., Yodh, A. G., Schnall, M., Chance, B. Concurrent MRI and Diffuse Optical Tomography of Breast After Indocyanine Green Enhancement. *Proc. Natl. Acad. Sci. USA 97*, 2767-2772 (2000).
57. Li, A., Miller, E. L., Kilmer, M. E., Brukilacchio, T. J., Chaves, T., Stott, J., Zhang, Q., Wu, T., Chorlton, M., Moore, R. H., Kopans, D. B., Boas, D. A. Tomographic Optical Breast Imaging Guided by Three-dimensional Mammography. *Appl. Opt. 42*, 5181-5190 (2003).
58. Zhu, Q., Conant, E., Chance, B. Optical Imaging as an Adjunct to Sonograph in Differentiating Benign from Malignant Breast Lesions. *J. Biomed. Opt. 5*, 229-236 (2000).
59. Brooksby, B., Jiang, S., Dehghani, H., Pogue, B. W., Paulsen, K. D., Weaver, J., Kogel, C., Poplack, S. P. Combining Near-infrared Tomography and Magnetic Resonance Imaging to Study *In Vivo* Breast Tissue: Implementation of a Laplacian-type Regularization to Incorporate Magnetic Resonance Structure. *J. Biomed. Opt. 10*, 051504 (2005).
60. Intes, X., Maloux, C., Guven, M., Yazici, B., Chance, B. Diffuse Optical Tomography with Physiological and Spatial *A Priori* Constraints. *Phys. Med. Biol. 49*, N155-63 (2004).
61. Gulsen, G., Yu, H., Wang, J., Nalcioglu, O., Merritt, S., Bevilacqua, F., Durkin, A. J., Cuccia, D. J., Lanning, R., Tromberg, B. J. Congruent MRI and Near-infrared Spectroscopy for Functional and Structural Imaging of Tumors. *Technol. Cancer Res. Treat. 1*, 497-505 (2002).
62. Brooksby, B., Srinivasan, S., Jiang, S., Dehghani, H., Pogue, B. W., Paulsen, K. D., Weaver, J., Kogel, C., Poplack, S. P. Spectral Priors Improve Near-infrared Diffuse Tomography More Than Spatial Priors. *Opt. Lett. 30*, 1968-1970 (2005).
63. Merritt, S., Bevilacqua, F., Durkin, A. J., Cuccia, D. J., Lanning, R., Tromberg, B. J., Gulsen, G., Yu, H., Wang, J., Nalcioglu, O. Coregistration of Diffuse Optical Spectroscopy and Magnetic Resonance Imaging in a Rat Tumor Model. *Appl. Opt. 42*, 2951-2959 (2003).
64. Cuccia, D. J., Bevilacqua, F., Durkin, A. J., Merritt, S., Tromberg, B. J., Gulsen, G., Yu, H., Wang, J., Nalcioglu, O. *In Vivo* Quantification of Optical Contrast Agent Dynamics in Rat Tumors by Use of Diffuse Optical Spectroscopy with Magnetic Resonance Imaging Coregistration. *Appl. Opt. 42*, 2940-2950 (2003).
65. Gulsen, G., Xiong, B., Birgul, O., Nalcioglu, O. Design and Implementation of a Multifrequency Near-infrared Diffuse Optical Tomography System. *J. Biomed. Opt. 11*, 14020 (2006).
66. Firbank, M., Oda, M., Delpy, D. T. An Improved Design for a Stable and Reproducible Phantom Material for Use in Near-infrared Spectroscopy and Imaging. *Phys. Med. Biol. 40*, 955-961 (1995).
67. Stoica, G., Koestner, A., Capen, C. C. Neoplasms Induced with High Single Doses of N-ethyl-N-nitrosourea in 30-day-old Sprague-Dawley Rats, with Special Emphasis on Mammary Neoplasia. *Anticancer Res. 4*, 5-12 (1984).
68. Su, M. Y., Wang, Z., Carpenter, P. M., Lao, X., Muhler, A., Nalcioglu, O. Characterization of N-ethyl-N-nitrosourea-induced Malignant and Benign Breast Tumors in Rats by Using Three MR Contrast Agents. *J. Magn. Reson. Imaging. 9*, 177-186 (1999).
69. McBride, T. O., Pogue, B. W., Osterberg, U. L., Paulsen, K. D. Strategies for Absolute Calibration of Near Infrared Tomographic Tissue Imaging. *Adv. Exp. Med. Biol. 530,* 85-99 (2003).
70. Wilson, B. C., Patterson, M. S. Future Directions and Applications in Photodynamic Therapy. *Proc. Soc. Photo-opt Instrum. Eng. 1506,* 219-231 (1990).
71. Schmidt, F. E. W., Fry, M. E., Hillman, E. M. C., Hebden, J. C., Delpy, D. T. A 32-channel Time-resolved Instrument for Medical Optical Tomography. *Rev. Sci. Instrum. 71,* 256 (2000).
72. Paulsen, K. D. and Jiang, H. Spatially Varying Optical Property Reconstruction Using a Finite Element Diffusion Equation Approximation. *Med. Phys. 22*, 691-701 (1995).
73. Jiang, H., Paulsen, K. D., Osterberg, U. L., Pogue, B. W., Patterson, M. S. Optical Image Reconstruction Using Frequency Domain Data: Simulations and Experiments. *J. Opt. Soc. Am. A. 13,* 253 (1996).
74. Bertero, M., Boccacci, P. *Introduction to Inverse Problems in Imaging*. Institute of Physics Publishing. (2002).
75. Srinivasan, S., Pogue, B. W., Dehghani, H., Jiang, S., Song, X., Paulsen, K. D. Improved Quantification of Small Objects in Near-infrared Diffuse Optical Tomography. *J. Biomed. Opt. 9*, 1161-1171 (2004).

76. Gribbestad, I. S., Nilsen, G., Fjosne, H., Fougner, R., Haugen, O. A., Petersen, S. B., Rinck, P. A., Kvinnsland, S. Contrast-enhanced Magnetic Resonance Imaging of the Breast. *Acta. Oncol. 31*, 833-842 (1992).
77. Pham, T. H., Hornung, R., Berns, M. W., Tadir, Y., Tromberg, B. J. Monitoring Tumor Response During Photodynamic Therapy Using Near-infrared Photon-migration Spectroscopy. *Photochem. Photobiol. 73*, 669-677 (2001).
78. Dehghani, H., Delpy, D. T., Arridge, S. R. Photon Migration in Non-scattering Tissue and the Effects on Image Reconstruction. *Phys. Med. Biol. 44*, 2897-2906 (1999).
79. Dehghani, H., Arridge, S. R., Schweiger, M., Delpy, D. T. Optical Tomography in the Presence of Void Regions. *J. Opt. Soc. Am. A. Opt. Image Sci. Vis. 17*, 1659-1670 (2000).
80. Xu, H., Zhang, Q., Jiang, H. Optical Image Reconstruction of Non-scattering and Low Scattering Heterogeneities in Turbid Media Based on the Diffusion Approximation Model. *J. of Opt. A: Pure and Applied Optics 6*, 29-35 (2004).
81. Gassan, S. A., Andreas, H. H. Three-dimensional Optical Tomography with the Equation of Radiative Transfer. *Journal of Electronic Imaging. 12*, 594-601 (2003).
82. Su, M. Y., Yu, H. J., Carpenter, P. M., McLaren, C. E., Nalcioglu, O. Pharmacokinetic Parameters Analyzed from MR Contrast Enhancement Kinetics of Multiple Malignant and Benign Breast Lesions Detected in the Same Patients. *Technol. Cancer Res. Treat. 4*, 255-263 (2005).
83. Gulsen, G., U. M. B., Birgul, O., Yan, H., Nalcioglu, O. A Multi-modality System for Dynamic Imaging of Cancer. *Proceedings of IEEE, International Symposium on Biomedical Imaging* (2006).

Received: April 19, 2006; Revised: July 8, 2006;
Accepted: July 8, 2006